Adaptive Impedance Control for an Upper Limb Robotic Exoskeleton Using Biological Signals

Zhijun Li, *Senior Member, IEEE*, Zhicong Huang, Wei He, *Member, IEEE*, and Chun-Yi Su, *Senior Member, IEEE*

***Abstract*—This paper presents adaptive impedance control of an upper limb robotic exoskeleton using biological signals. First, we develop a reference musculoskeletal model of the human upper limb and experimentally calibrate the model to match the operator's motion behavior. Then, the proposed novel impedance algorithm transfers stiffness from human operator through the surface electromyography (sEMG) signals, being utilized to design the optimal reference impedance model. Considering the unknown deadzone effects in the robot joints and the absence of the precise knowledge of the robot's dynamics, an adaptive neural network control incorporating with a high-gain observer is developed to approximate the deadzone effect and robot's dynamics and drive the robot tracking desired trajectories without velocity measurements. In order to verify the robustness of the proposed approach, the actual implementation has been performed using a real robotic exoskeleton and a human operator.**

***Index Terms*—Adaptive impedance control, high-gain observer, neural networks, robotic exoskeleton.**

Nomenclature

$u_i(t)$	Processed sEMG signal of ith muscle.
$a_i(t)$	Activation of the ith muscle.
$F_i^{mt}(t)$	Total force generated by the muscle–tendon.
$F_i^{\max}$	Maximum isometric force of ith muscle.
$f_i(l_i)$	Normalized force–length function.
$f_i(v_i)$	Normalized force–velocity function.
$f_{pi}(l_i)$	Normalized force–length function.
$\psi_i(t)$	Pennation angle.
$F_i^t(t)$	Tendon force.
l_i	Normalized muscle fiber length.
v_i	Normalized muscle fiber velocity.
$F_{ai}^m(t)$	Contractile element produces active force.
$F_{pi}^m(t)$	Parallel elastic produces passive force.
$l_i^m(t)$	Muscle fiber length.
ψ_{oi}	Pennation angle at the muscle fiber length.
l_{oi}^m	Optimal muscle fiber length.
$l_{oi}'^m$	Optimal fiber length at maximum activation.
γ	Percentage change in optimal fiber length.
l_{si}^t	Tendon slack length.
$l_i^t(t)$	Tendon length.
$l_i^{mt}(t)$	Muscle–tendon length.
θ_i	Corresponding joint angle.
$r_{ai}(t)$	Moment arms of the musculotendonous.
$\tau_{\text{joint}}(t)$	Joint torques.
$K_l(t)$	Joint stiffness.
$C_l(t)$	Joint viscosity.
$f_{ej}(j{=}x, y, z)$	Generated forces in each direction.
$\Delta f_{ej}(j{=}x, y, z)$	Incremental forces.
$A^{\text{anta}-i}$	Preprocessed antagonist sEMG signals.
$\Delta A^{\text{anta}-i}$	Incremental antagonist sEMG signals.
$A^{\text{ago}-i}$	Preprocessed agonist sEMG signals.
$\Delta A^{\text{ago}-i}$	Incremental agonist sEMG signals.
$r_{ej}(j{=}x, y, z)$	Residual errors caused by nonlinear factors.
$\Delta r_{ej}(j{=}x, y, z)$	Incremental residual errors.
$K_{jj}(j{=}x, y, z)$	endpoint stiffness of the human arm.
$\Delta K_{jj}(j{=}x, y, z)$	Incremental stiffness.
$r_f^j(j{=}x, y, z)$	Nonlinear residual errors.
$\Delta r_f^j(j{=}x, y, z)$	Incremental nonlinear residual errors.
$K_P(t)$	Stiffness matrix.
K_J	Transferred joint impedance from human.
J_j	Jacobian matrix

Manuscript received November 12, 2015; revised January 17, 2016; accepted February 5, 2016. Date of publication March 4, 2016; date of current version January 10, 2017. This work was supported in part by the National Natural Science Foundation of China under Grant 61573147 and Grant 91520201, in part by Guangzhou Research Collaborative Innovation Projects under Grant 2014Y2-00507, in part by Guangdong Science and Technology Research Collaborative Innovation Projects under Grant 2014B090901056, in part by Guangdong Science and Technology Plan Project (Application Technology Research Foundation) under Grant 2015B020233006, and in part by the National High-Tech Research and Development Program of China (863 Program) under Grant 2015AA042303. *(Corresponding author: Zhijun Li).*

Z. Li and Z. Huang are with the College of Automation Science and Engineering, South China University of Technology, Guangzhou 510641, China (e-mail: zjli@ieee.org; zhiconghuang1@163.com).

W. He is with the School of Automation and Electrical Engineering, University of Science and Technology Beijing, Beijing 100083, China (e-mail: hewei.ac@gmail.com).

C.-Y. Su is with the College of Automation Science and Engineering, South China University of Technology, Guangzhou 510641, China, and also with the Department of Mechanical and Industrial Engineering, Concordia University, Montreal, QC H4B 1R6, Canada (e-mail: cysu@alcor.concordia.ca).

Color versions of one or more of the figures in this paper are available online at http://ieeexplore.ieee.org.

Digital Object Identifier 10.1109/TIE.2016.2538741

I. Introduction

POWERED exoskeletons have attracted much attention over the past few years and can be applied from military usage to patient rehabilitation [1] –[4]. The

exoskeletons are developed to augment the human's muscular force and endurance in carrying heavy loads. Compared with rehabilitation exoskeletons which recover the neuromusculoskeletal function of stroke or postsurgical patients, assistive exoskeletons can assist the elderly or individuals with mobility disorders during demanding, in terms of power, motion tasks. The exoskeletons can not only perform the cooperation with the humans but also assist or supplement the human motion. Therefore, it is necessary that the developed exoskeletons could exhibit biological behavior and performance.

Considering human joints, one of the important features is the physical properties of the musculotendinous and their resultant impedance. In particular, several biomechanical studies of human movement reported that the impedance profiles of the human joints vary substantially during motion [5], [6]. Therefore, exoskeletons should accordingly respond and adapt to these impedance profiles. In this manner, their utilization becomes more effective and intuitive, while the agility and comfort of the operator wearing the device are significantly increased. Therefore, many efforts should be made into employing variable impedance property into exoskeletons, orthoses, or prostheses such that naturally human-like mechanics can be produced [12], [13]. However, it is a highly challenging task for planning impedance profiles of these wearing devices since only indirect approaches such as modeling, body state, or offline optimization techniques can be applied. For instance, in [14], the recursive least-square (RLS) method was employed to estimate joint impedance for HAL exoskeleton. In [15], the authors proposed a muscle model by utilizing anatomical and physiological data from EMG, where muscle tension can be described with a quadratic function of the muscle activation, and the joint stiffness can be directly obtained by differentiation of this model analytically. In [16], a method called as tele-impedance was proposed for controlling a robotic arm interacting with uncertain environments, which decoupled the estimations of force and stiffness of the human arm. In [17], the authors designed an interface between the operator and the exoskeleton by using the muscle signals, and the biomechanical parameters in the human model are identified-based geometry calibration. Motivated by the previous works [7], [18], impedance control has been extensively investigated, which adjusts the mechanical impedance specified by a target model. Based on the previous work [19] and considering unknown dynamics [20], in this paper, we present adaptive impedance control of the exoskeleton joint based on stiffness measurements of the corresponding joint of the operator. Therefore, it is necessary to build a model of musculoskeletal bio-feedbacks.

Neural network (NN) is powerful in controller design for uncertain dynamical systems, which has been verified in [8]–[11], [21]. Different from model-based approaches, neural network control methods are considered as approximation-based methods and do not require parametric or functional certainties. By an inherent learning ability of the neural network for nonlinear dynamics, it is desirable to apply it to the control of robotic exoskeletons with an important advantage that the dynamics of the robotic exoskeleton do not need to be completely known as a prior condition. It would be an attractive feature in designing the controller. For example, in [7], the neural network controller by approximating the manipulator uncertainties was introduced to handle the input saturation and achieve the tracking trajectory. In [8], a feedforward neural network was utilized to learn the unknown dynamics of robot manipulators and the grasped object. In [9], a neural network compensator approximates the dynamics of the underwater vehicle-manipulator systems in decentralized form. In [10], the control design of multiple-legged robotic system was proposed by using the fuzzy logic systems and neural-dynamics approximation, and through the adaptive fuzzy logic control law, the tracking error of each leg converges to an adjustable neighborhood of zero. In [11], intelligent control approach for a dual-arm wheeled mobile manipulator incorporates sliding-mode control (SMC) and fuzzy neural network (FNN) for a path-tracking problem of the dual-arm wheeled mobile manipulator subject to dynamic uncertainties and nonholonomic constraints.

Therefore, this paper presents adaptive impedance control for an upper limb robotic exoskeleton using biological signals. First, we develop a reference musculoskeletal model of the human upper limb and experimentally calibrate the model to match the operator's motion behavior. Then, the proposed novel impedance algorithm transfers stiffness from human operator through the surface electromyography (sEMG) signals, which is utilized to design the optimal reference impedance model. Considering the unknown deadzone effects in the robot joints and the absence of the precise knowledge of the robot's dynamics, an adaptive neural network control incorporating with a high-gain observer is developed to approximate the deadzone effects and robot's dynamics and drive the robot tracking the desired trajectories without velocity measurements. In order to verify the robustness of the proposed approach, the actual implementation has been performed using a real robotic exoskeleton and a human operator.

The contributions can be summarized as follows.

1) A reference musculoskeletal model of the human upper limb is developed and experimentally calibrated to match the operator's kinematic and dynamic behavior.
2) Novel impedance algorithm transfers stiffness from human operator through the sEMG signals, and being utilized to design the optimal reference impedance model for the robot system.
3) Considering the unknown deadzone effects in the robot joints and the absence of the precise knowledge of the robot's dynamics, an adaptive neural network control incorporating with high-gain observer is developed to approximate the deadzone effects and robot's dynamics and drive the robot to track the desired trajectories without velocity measurements.

II. sEMG-Driven Musculoskeletal Model

This section describes the sEMG-driven musculoskeletal model of the human forearm's joints, which is used to account for the net torque and joint stiffness trend index (STI), which is shown in Fig. 1.

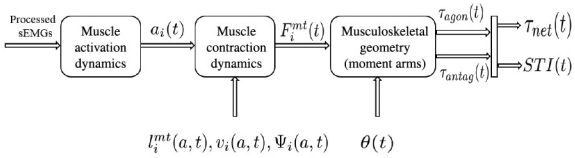

Fig. 1. Musculoskeletal model deriving the net torque and the STI.

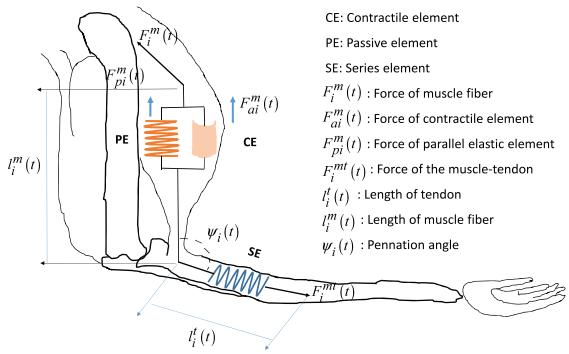

Fig. 2. Human muscle model.

A. Activation Dynamics

The sEMG signals inherit patterns of activations of involved muscles. In this paper, let $u_i(t)$ as the processed sEMG signal of ith muscle. From [15], it is well known that muscle force variations with respect to neural commands can be described as follows:

$$a_i(t) = \frac{e^{Au_i(t)-1}}{e^A - 1} \tag{1}$$

where $a_i(t)$ denotes activation of the ith muscle, and $-3 < A < 0$ is a nonlinear shape factor.

B. Contraction Dynamics

Human muscles have been modeled based on Hill's muscle model in [15]. The muscle force can be produced by muscle visco-elasticity and reflexes through muscle activation and contraction dynamics, while the muscle–tendon unit can be modeled by a muscle fiber and a viscoelastic tendon, which is shown in Fig. 2, where muscle fiber itself can be described as a contractile element in parallel with an elastic component. Then, the total force $F_i^{mt}(t)$ generated by the muscle–tendon can be presented as

$$F_i^{mt}(t) = F_i^{\max}[f_i(l_i)f_i(v_i)a_i(t) + f_{p_i}(l_i)]\cos(\psi_i(t)) \tag{2}$$

where $F_i^{mt}(t) = F_i^t(t)$, $F_i^t(t)$ is the tendon force, with $f_i(l_i)$ and $f_i(v_i)$ denoting normalized force–length and normalized force–velocity curves of the contractile element of ith muscle, and $f_{pi}(l_i)$ denotes the passive elastic normalized force–length relation, $F_i^{\max}$ denotes the maximum isometric force of ith muscle, l_i is the normalized muscle fiber length, and v_i is the normalized muscle fiber velocity [22], [23].

The contractile element produces active force $F_{ai}^m(t) = f_i(l_i)f_i(v_i)a_i(t)F_i^{\max}$, parallel elastic produces passive force $F_{pi}^m(t) = f_{pi}(l_i)F_i^{\max}$. The angle between the tendon and the muscle fibers is the pennation angle $\psi_i(t)$, and could be obtained by

$$\psi_i(t) = \sin^{-1}\left(\frac{l_{oi}^m \sin(\psi_{oi})}{l_i^m(t)}\right) \tag{3}$$

where $l_i^m(t)$ denotes the muscle fiber length and ψ_{oi} is the pennation angle at the optimal muscle fiber length l_{oi}^m.

In order to calculate (2), some simplifications have been already proposed to replace the complex biomechanical parameters [24], i.e.,

$$f_i(l_i) = \begin{cases} q_0 + q_1 \cdot l_i + q_2 \cdot l_i^2, & 0.5 \le l_i \le 1.5 \\ 0, & \text{otherwise} \end{cases} \tag{4}$$

where $q_0 = -2.06$, $q_1 = 6.16$, and $q_2 = -3.13$ are set to be constants, and let $f_{pi}(l_i) = e^{10 \cdot l_i - 15}$, $f_i(v_i) = 1$, according to the force–length curve-fitting algorithm depicted in [23] and [25].

According to the previous work [26], the optimal muscle fiber length increases as the muscle activation decreases. To take into account this dependency of optimal muscle fiber length on activation fluctuations, we adopt the relationship as

$$l_{oi}^m(t) = l_{oi}'^m(\gamma(1 - a_i(t)) + 1) \tag{5}$$

where $l_{oi}'^m$ denotes the optimal fiber length at maximum activation, and γ denotes the percentage change in optimal fiber length, chosen to be 15% [23]. It is well known that a linear relationship exits between the tendon slack length l_{si}^t, tendon force, and the tendon length $l_i^t(t)$. Such mapping is valid for $l_i^t(t) > l_{si}^t$. Here, similar assumptions have been made in modeling the tendon length. Moreover, we have

$$l_i^t(t) = l_i^{mt}(t) - l_i^m(t)\cos(\psi_i(t)) \tag{6}$$

with $l_i^{mt}(t)$ denoting the muscle–tendon length.

In order to simplify the model and reduce the complexity of the calculation, the physiological parameters of $(F_i^{\max}, l_i^t(t), l_{oi}^m, \psi_i(t))$ can also be set as constants. Thus, once the musculotendon length of $l_i^{mt}(t)$ and the constants of $(F_i^{\max}, l_i^t(t), l_{oi}^m, \psi_i(t))$ are known, we could calculate $l_i^m(t)$ by (6), and finally, calculate the musculotendon force by (2).

C. Musculoskeletal Geometry

The length of the muscle–tendon complexes acting on the forearm joint can be the functions of the corresponding joint angle, and the muscle length values can be fitted to a first-order polynomial. Considering the upper limb geometry, we define the following function:

$$l_i^{mt}(t) = b_{0i} + b_{1i}\theta_i \tag{7}$$

where θ_i refers to the corresponding joint angle, b_{0i} and b_{1i} are constants. By adopting (5)–(7), the muscle fiber length can be identified and utilized for the estimation of the contraction dynamics.

The moment arms $r_{ai}(t)$ of the corresponding musculotendonous unit could be described based on the displacements method proposed in [27]; we have

$$r_{ai}(t) = \frac{\partial l_i^{mt}(t)}{\partial \theta_i}. \tag{8}$$

Based on the estimated forces (2) and the moment arms (8) of all selected muscles acting on the joint, the muscle forces could be converted to joint torques $\tau_{\text{joint}}(t)$ by using

$$\tau_{\text{joint}}(t) = \left|\sum_{i=1}^{n} \tau_i(t)\right|_{\text{agonist}} - \left|\sum_{i=1}^{n} \tau_i(t)\right|_{\text{antagonist}} \tag{9}$$

where $\tau_i(t) = F_i^{mt}(t) r_{ai}(t)$, n is the number of agonistic/antagonistic muscle pairs acting on the joints.

It has been observed that a simultaneous increase in antagonistic muscle torques acting on the joint does not influence the joint torque [as seen in (9)] though it does increase joint stiffness. Consequently, the STI can be defined by

$$\text{STI}(t) = \left|\sum_{\text{agonist}} \tau_i(t)\right| + \left|\sum_{\text{antagonist}} \tau_i(t)\right| \tag{10}$$

and the stiffness of the joint is written as

$$K_l(t) = \alpha_l \times \text{STI}(t) + \beta_l. \tag{11}$$

The stiffness of the forearm joints is shown to be functions of STI. In this paper, the stiffness could be fitted to a first-order polynomial, where both α_l (rad) and β_l (Nm/rad) are constants which need to be identified. The stiffness K_l could be acquired through the linear mapping between muscle sEMG signal amplitude and human arm stiffness; the linear mapping relationship is described at Section II-D.

When the endpoint stiffness is estimated, the joint viscosity can be calculated by the joint stiffness K_l. In previous work [29], from the relationships between joint stiffness K_l and its viscosity C_l, the experimental data suggested that the damping ratio was constant despite of cocontraction, which demonstrated a linear relationship between square-root joint stiffness and joint viscosity. Therefore, joint viscosity C_l can be selected as

$$C_l = \nu\sqrt{K_l}. \tag{12}$$

The constant ν can be tuned to adjust the damping of the system.

D. Simplification of Human Arm Stiffness

As we all know, sEMG is highly related to the static/dynamic stiffness and the skeletal muscle tensions. Based on the fact that the sEMG is highly related to the static stiffness [28], and the generated stiffness is highly related to the generated torque [29], we assume that the relationship is linear for the simplification and the moment arms are considered as constants around the operational space in this paper. It shows that the correlation of rectified sEMG and force is approximately linear.

According to [30] and [31], the linear relationship between sEMG amplitude and the endpoint forces can be shown as

$$f_{ej} = \sum_{i=1}^{n} \alpha_{i,j} \cdot A^{\text{ago}-i} - \sum_{i=1}^{n} \beta_{i,j} \cdot A^{\text{anta}-i} + r_{ej} \tag{13}$$

where f_{ej} ($j = x$, y, or z) denotes the generated forces at the human arm endpoint in x-, y-, and z-directions, respectively, n is the number of DOF in operational space, and $A^{\text{anta}-i}$ and $A^{\text{ago}-i}$ are preprocessed antagonist/agonist sEMG signals, and the coefficients $\alpha_{i,j}$, $\beta_{i,j}$ are all constants to be estimated, and r_{ej} ($j = x$, y, or z) is the residual error caused by nonlinear factors. Through asking the subject to apply the force or maintain the given force along six directions, the subject's sEMG signals can be collected. According to the above equations, we could calculate the values of $(\alpha_{i,j}, \beta_{i,j})$ by means of least-square-error approach.

In order to reduce the effect of the residual errors and simplify the nonlinearity, incremental forces estimation is introduced by taking a first-order difference of the above equation [31]

$$\Delta f_{ej} = \sum_{i=1}^{n} \alpha_{i,j} \cdot \Delta A^{\text{ago}-i} - \sum_{i=1}^{n} \beta_{i,j} \cdot \Delta A^{\text{anta}-i} + \Delta r_{ej} \tag{14}$$

where $\Delta f_{ej} = f_{ej}(t+1) - f_{ej}(t)$ with ($j = x$, y, or z) is incremental force; $\Delta A^{\text{ago}-i} = A_{t+1}^{\text{ago}-i} - A_t^{\text{ago}-i}$; $\Delta A^{\text{anta}-i} = A_{t+1}^{\text{anta}-i} - A_t^{\text{anta}-i}$; $\Delta r_{\text{ex}} = r_{ex}(t+1) - r_{ex}(t) \approx 0$, $\Delta r_{ey} = r_{ey}(t+1) - r_{ey}(t) \approx 0$, $\Delta r_{ez} = r_{ez}(t+1) - r_{ez}(t) \approx 0$, where t and $t+1$ are current and one step further sampling instants. The relationship between limb endpoint forces and sEMG signals of agonist/antagonist muscles is described by (13). Thus, we can calculate $f_{ej}(t)$ through the accumulation of the incremental stiffness on the time interval $[0, t]$, $f_{ej}(t) = \sum_0^t \Delta f_{ej}$.

As we all know, the muscle stiffness is approximately proportional to muscle torque [30], [32]. Therefore, the measurement of human arm endpoint stiffness could be the total of the absolute values of numerous skeletal muscle torques. The specific stiffness estimation can be described as

$$K_{jj} = \sum_{i=1}^{n} |\alpha_{i,j}| \cdot A^{\text{ago}-i} + \sum_{i=1}^{n} |\beta_{i,j}| \cdot A_t^{\text{anta}-i} + r_f^j \tag{15}$$

where K_{jj} ($j = x$, y, or z) denotes endpoint stiffness of the human arm, and r_f^j denotes the nonlinear residual errors.

In this paper, a simplification model is adopted to estimate human-arm incremental stiffness (16) to overcome possible nonlinear residual items if the robot original stiffness is higher than the stiffness estimated from human muscle, some possible accident caused by sudden fall of stiffness on robot would be avoided. So, the calibration is necessary for the initialization of human–robot interaction. Incremental stiffness estimation is introduced as

$$\Delta K_{jj} = \sum_{i=1}^{n} |\alpha_{i,j}| \cdot \Delta A^{\text{ago}-i} + \sum_{i=1}^{n} |\beta_{i,j}| \cdot \Delta A_t^{\text{anta}-i} + \Delta r_f^j \tag{16}$$

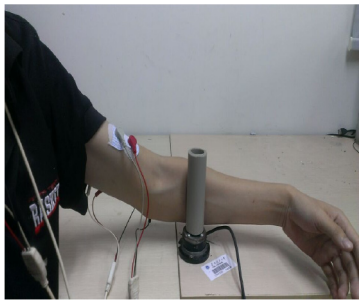

Fig. 3. Force sensor used in the experiment.

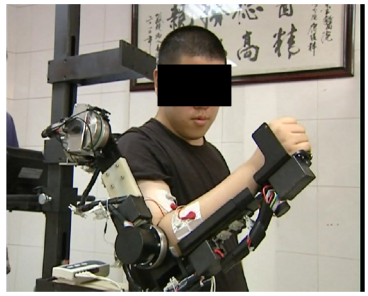

Fig. 4. Upper limb exoskeleton robot.

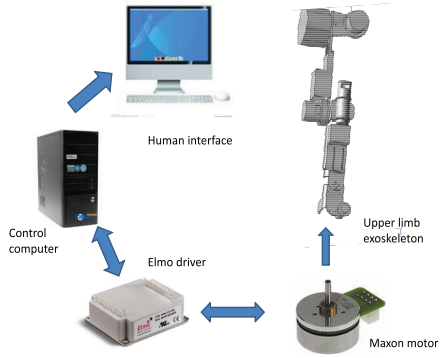

Fig. 5. Upper limb exoskeleton platform.

where $\Delta K_{jj} = K_{jj}(t+1) - K_{jj}(t)$ with $j = x,\ y,$ or z is incremental stiffness; $\Delta A^{\text{ago}-i} = A_{t+1}^{\text{ago}-i} - A_t^{\text{ago}-i}$; $\Delta A^{\text{anta}-i} = A_{t+1}^{\text{anta}-i} - A_t^{\text{anta}-i}$; $\Delta r_f^x = r_f^x(t+1) - r_f^x(t) \approx 0$, $\Delta r_f^y = r_f^y(t+1) - r_f^y(t) \approx 0$, $\Delta r_f^z = r_f^z(t+1) - r_f^z(t) \approx 0$. The signal-processing method used to detect instantaneous amplitude $A_t^{\text{ago}-i}$ and $A_t^{\text{anta}-i}$ will be detailed in Section II-E. Thus, we can calculate $K_{jj}(t)$ through the accumulation of the incremental stiffness on the time interval $[0, t]$, $K_{jj}(t) = \sum_0^t \Delta K_{jj}$. Finally, we calculate stiffness matrix as

$$K_P(t) = \text{diag}[K_{xx}(t), K_{yy}(t), K_{zz}(t)]. \tag{17}$$

Although the above method would unavoidably bring precision and estimation errors, since relevant task is executed in the vicinity of the posture in which the related parameters are estimated, this method is still able to provide the intensive properties of the endpoint stiffness profile. Let

$$K_J = \text{diag}[K_{J1}, \ldots, K_{Jn}] \tag{18}$$

where $K_{Ji} > 0, i = 1, \ldots, n$, is the transferred joint impedance from human operator, and the joint stiffness K_J used in the control law of the exoskeleton robot is obtained by coordinate transformation from operational space by using Jacobian matrix J_j, i.e., $K_J = J_j^T K_P J_j$, where K_P is defined in (17).

E. Stiffness Model Calibration

In order to calibrate the stiffness model in (13)–(16), we perform a stiffness calibration experiment. One healthy human subject (male, 55 kg, 170 cm, and 24 years) provided the informed consent and participated in the experiment. The subject sits upright ahead of the cylindrical joint shown in Fig. 3, which is designed for reducing undesired generated torques of the subject's wrist. The joint is equipped with a 6-axis force torque sensor (SRI-M3203). With visual feedback and isometric criteria, the subject was asked to apply the force or maintain the force at 4 N, 8 N, 12 N, and 16 N along four directions $[\pm X, \pm Y]$ and along the $\pm Z$-directions. The subject conducted this experiment three times for the estimation of the parameters in (13).

During experiments, sEMG data from four muscles were obtained by using surface electrodes. The signals are sampled at 1024 Hz, bandpass filtered between 10 and 500 Hz, and notch filtered at 50 Hz. All the filters are all butterworth filters and implemented in software. Furthermore, the maximum voluntary contraction (MVC) values are used to normalize to the extracted signals with the purpose of having extracted signals analogous to muscle activations. The endpoint force and four muscle activations are recorded during the experiments, and the parameters of (13) are estimated by means of least-square-error approach with 72 trial data as results. Further, the absolute values of these parameters are used for the construction of cocontraction-based index of endpoint stiffness profile as in (15). We followed the above steps and calculated the parameters of (13) and estimated stiffness of endpoint in X-, Y-, Z-directions.

The limb of the subject is in tight during 5–13 s, and at the rest of time, the limb is on the relax situation. We can see the obvious changes of endpoint stiffness, since the blue thick line is the average stiffness of X-, Y-, Z-directions during five tasks. Further, in order to calculate the Jacobian matrix and get the joint stiffness, the specific motors in the arm of exoskeleton robot are set to move at sinusoidal trajectory without disturbance. After transformation, we can obtain the joint stiffness which are shown in Figs. 7 and 8.

III. System Description

A. System Development

The robotic exoskeleton consisting of 5-DOF robotic exoskeleton has been developed for the experiments in SCUT lab, as shown in Figs. 4 and 5. There are five revolute joints in the each developed robotic arm. The robotic exoskeleton is developed using dc motors as actuators, and Maxon dc flat brushless motor EC45 is chosen as driver unit. The robotic exoskeleton platform includes the four-layer control architecture as robotic exoskeleton, distributed embedded system (Elmo

driver), servo motor, and control computer. The position, angular velocity needed for control can be read from the joint sensors and the power signals are generated to activate the actuators nominally running at 1 kH.

B. Dynamics of Exoskeleton

The dynamics of an n-link rigid robotics exoskeleton with deadzone could be described as

$$M(q)\ddot{q} + C(q,\dot{q})\dot{q} + G(q) + f_{\text{dis}}(t) = D(\tau) \tag{19}$$

where $q \in \mathbb{R}^n$ is the coordinate of the robotic exoskeleton and n denotes the DOF; $\boldsymbol{\tau} \in \mathbb{R}^n$ is the desired control input vector (joint torque applied) and $D(\tau)$ is the deadzone nonlinear function to the desired control inputs τ due to motor's imperfection; $M(q) \in \mathbb{R}^{n\times n}$ is a symmetric positive definite inertia matrix; $C(q,\dot{q}) \in \mathbb{R}^n$ is the Coriolis and centrifugal torques; $G(q) \in \mathbb{R}^n$ is the gravitational force vector; and $f_{\text{dis}}(t) \in \mathbb{R}^n$ is the external disturbance vector to the exoskeleton.

Property 1: [33] The matrix $\dot{M}(q) - 2C(q,\dot{q})$ is skew-symmetric.

Assumption 1: We assume that external disturbance $f_{\text{dis}}(t)$ is uniformly bounded. Namely, there exists a vector $\bar{f} \in \mathbb{R}^{n+}$, such that $f_{\text{dis}}(t) < \bar{f}\ \forall t \in [0,\infty)$.

Assumption 2: The deadzone nonlinearity could be described as

$$D(\tau) = \begin{cases} h_r(\tau - b_r), & \tau \geq b_r \\ 0, & b_l < \tau < b_r \\ h_l(\tau - b_l), & \tau \leq b_l \end{cases} \tag{20}$$

where for vector $\{X\}$, $X \in \mathbb{R}^{1\times n}$, $D(X) = [D(x_1), D(x_2), \ldots, D(x_n)]$, the deadzone parameters b_r and b_l are unknown constants that meet the condition that $b_r > 0$ and $b_l < 0$.

Assumption 3: For the unknown smooth function $h_r(\cdot)$ and $h_l(\cdot)$, there always exist unknown positive constants H_0 and H_1, which satisfy the following inequations:

$$0 < H_{r0} < \dot{h}_r(\tau - b_r) < H_{r1}, \quad \tau \in [b_r, +\infty) \tag{21}$$

$$0 < H_{l0} < \dot{h}_l(\tau - b_l) < H_{l1}, \quad \tau \in (-\infty, b_l]. \tag{22}$$

Assumption 4: The desired trajectory q_d is continuous and known.

C. Optimal Reference Model and Model Matching Errors

First, we design an impedance model with virtual force, which can be described as

$$M_r\ddot{q} + C_r\dot{q} + K_r q = -F_r(q_d, \dot{q}_d) \tag{23}$$

where M_r is the desired inertia, C_r is the desired damping, K_r denotes the desired stiffness matrices, and F_r could be considered as a virtual torque.

The given impedance model is achieved by the identification of the human arm model, the desired damping and stiffness C_r, K_r can be substituted by joint viscosity and stiffness C_l, K_l of the human forearm, and the virtual torque can be substituted by the joint torque τ_{joint}. By using $e = q - q_d$, the reference model (23) can be rewritten as

$$M_r\ddot{e} + C_r\dot{e} + K_r e = -\eta \tag{24}$$

where $\eta = F_r + M_r\ddot{q}_d + C_r\dot{q}_d + K_r q_d$. The control objective can be presented to find an appropriate control input torque τ such that the robot dynamics can match the desired reference model dynamics. Considering the difference between the system dynamics and the reference model dynamics, we can define the following matching error as

$$\omega = M_r\ddot{e} + C_r\dot{e} + K_r e + \eta \tag{25}$$

such that, while the matching error meet $\omega(t) = 0$, the system dynamics (19) would precisely match the desired reference model dynamics (24). To facilitate the following analysis, the augmented matching error is introduced as follows:

$$\bar{\omega} = K_\eta\omega = \ddot{e} + C_m\dot{e} + K_m e + K_\eta\eta \tag{26}$$

where $C_m = M_r^{-1}C_r$, $K_m = M_r^{-1}K_r$, and $K_\eta = M_r^{-1}$.

Remark 1: The virtual mass matrix M_r must be chosen to be positive definite such that it is invertible and $\bar{\omega}$ is well defined.

Choosing two appropriate positive-definite matrices Λ and Γ, satisfying $\Lambda + \Gamma = C_m$ and $\Gamma\Lambda + \dot{\Lambda} = K_m$, the augmented matching error $\bar{\omega}$ can be rewritten as

$$\bar{\omega} = \ddot{e} + (\Lambda + \Gamma)\dot{e} + (\Gamma\Lambda + \dot{\Lambda})e + \dot{\eta}_l + \Gamma\eta_l \tag{27}$$

where η_l satisfies $\dot{\eta}_l + \Gamma\eta_l = K_\eta\eta$. Considering a filtered matching error as

$$r = \dot{e} + \Lambda e + \eta_l \tag{28}$$

then we can rewrite the augmented matching error $\bar{\omega}$ as

$$\bar{\omega} = \dot{r} + \Gamma r. \tag{29}$$

IV. Control Design and Its Stability

A. Controller Structure

We assume that full-state information q and $\dot{q}$ are available. According to (19), if we let $x_1 = [q_1, q_2, q_3, \ldots, q_n]^T$, $x_2 = [\dot{q}_1, \dot{q}_2, \dot{q}_3, \ldots, q_n]^T$, then the robotics dynamics could be described as

$$\dot{x}_1 = x_2 \tag{30}$$

$$\dot{x}_2 = M^{-1}[D(\tau) - f_{\text{dis}} - G - Cx_2]. \tag{31}$$

Then, we define $\dot{q}_r$ and $\ddot{q}_r$ as $\dot{q}_r = \dot{q}_d - \Lambda e - \eta_l$, $\ddot{q}_r = \ddot{q}_d - \Lambda\dot{e} - \dot{\eta}_l$. According to (28), we could get $\dot{q} = \dot{q}_r + r, \ddot{q} = \ddot{q}_r + \dot{r}$. We define the variables z_1, z_2 as follows: $z_1 = x_1 - q_d$, $z_2 = x_2 - \dot{q}_r$. For the case of n-DOF robot manipulator, $\dot{q}_r \in \mathbb{R}^n$, $z_1 \in \mathbb{R}^n$, and $z_2 \in \mathbb{R}^n$.

$$\dot{z}_1 = \dot{x}_1 - \dot{q}_d = z_2 + \dot{q}_r - \dot{q}_d = \dot{e} = z_2 - \Lambda z_1 - \eta_l. \tag{32}$$

From the above equations, we could obtain

$$z_2 = r + \dot{q}_r - \dot{q}_r = r. \tag{33}$$

Consider Lyapunov function candidate $V_1 = \frac{1}{2} z_1^T z_1$. Time derivative of V_1 is

$$\dot{V}_1 = z_1 \dot{z}_1 = z_1^T (z_2 - \Lambda z_1 - \eta_l). \tag{34}$$

Then, we have

$$\dot{z}_2 = \dot{r} = M^{-1}[D(\tau) - f_{\text{dis}} - G - Cx_2] - \ddot{q}_r. \tag{35}$$

Let $D(\tau) = \tau - \Delta\tau$, where $\Delta\tau$ denotes the error. $V_2 = V_1 + \frac{1}{2} z_2^T M z_2$, so time derivative of V_2 will be

$$\begin{aligned}\dot{V}_2 =& \dot{V}_1 + z_2^T M \dot{z}_2 + \frac{1}{2} z_2^T \dot{M} z_2 \\ =& z_1^T (z_2 - \Lambda z_1 - \eta_l) + z_2^T (\tau - \Delta\tau \\ & - f_{\text{dis}} - G - Cx_2 - M\ddot{q}_r + \frac{1}{2}\dot{M} z_2 \Big).\end{aligned} \tag{36}$$

Applying Property 1, we have

$$\dot{V}_2 = z_1^T (z_2 - \Lambda z_1 - \eta_l) + z_2^T (\tau - \Delta\tau - f_{\text{dis}} - G - C\dot{q}_r - M\ddot{q}_r) \tag{37}$$

since we cannot have the exact information of $\Delta\tau$, and the external disturbance and the robotic dynamics. For solving this problem, we exploit radial basis function neural network (RBFNN) to approximate the unknown function as follows, then we have

$$\tau = -z_1 - K_2 z_2 + \hat{W}_\tau^T S_\tau(Z_\tau) + \hat{W}^T S(Z) + \bar{f}. \tag{38}$$

The neural network updating law is designed as $\dot{\hat{W}} = -\Gamma \left(S(Z) z_2 + \theta \hat{W} \right)$, $\dot{\hat{W}}_\tau = -\Gamma_\tau \left(S_\tau(Z_\tau) z_2 + \theta_\tau \hat{W}_\tau \right)$, where $K_2 \in \mathbb{R}^{n \times n}$, and $\lambda_{\min}(K_2) > 0$, θ and θ_τ are small positive real numbers, $\Gamma = \Gamma^T > 0$ and $\Gamma_\tau = \Gamma_\tau^T > 0$. $\hat{W}_\tau^T S_\tau(Z_\tau)$ is an approximation of $W_\tau^{*T} S_\tau(Z_\tau)$, and $\hat{W}^T S(Z)$ is an approximation of $W^{*T} S(Z)$.

$$W_\tau^{*T} S_\tau(Z_\tau) = \Delta\tau - \epsilon_\tau \tag{39}$$

$$W^{*T} S(Z) = G(x_1) + C(x_1, x_2)\dot{q}_r + M\ddot{q}_r - \epsilon \tag{40}$$

where W^{*T} and W_τ^{*T} are optimal weights, $S_\tau(Z_\tau)$ and $S(Z)$ are basis functions of the neural networks, ϵ and ϵ_τ are approximation errors of the neural networks, and $Z = [x_1^T, x_2^T, \dot{q}_r^T, \ddot{q}_r^T]$, $Z_\tau = [\tau^T, x_1^T, x_2^T]$.

Some variables in (38) may not be measurable. In order to solve this problem, a high-gain observer [34] is employed to estimate the unmeasurable terms. According to [33] and [21], the unmeasurable state x_2 can therefore be approximated as $\frac{\pi_2}{\gamma}$. The estimation of the unmeasurable state vector z_2 is given as

$$\hat{z}_2 = \pi_2/\varepsilon - \dot{q}_r \tag{41}$$

where the dynamics of π_2 are expressed as

$$\varepsilon \dot{\pi}_1 = \pi_2, \quad \varepsilon \dot{\pi}_2 = -\bar{\lambda}_1 \pi_2 - \pi_1 + x_1 \tag{42}$$

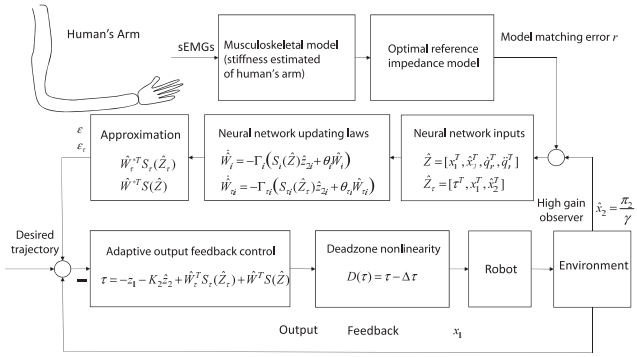

Fig. 6. Output feedback control strategy.

where ε is any small constant. According to [33], there exist positive constants t^* and r_n such that $\forall t > t^*$, we have $|\xi_2| \leq \varepsilon r_n$. So, $\tilde{z}_2$ can be estimated as follows:

$$\xi_2 = \frac{\pi_2}{\varepsilon} - \dot{x}_1 = -\varepsilon \psi^{(2)} \tag{43}$$

$$\tilde{z}_2 = \hat{z}_2 - z_2 = \frac{\pi_2}{\varepsilon} - \dot{q}_r - \dot{x}_1 + \dot{q}_r = \xi_2. \tag{44}$$

Then, we rewrite the control in (38) and neural network updating law as follows:

$$\tau = -z_1 - K_2 \hat{z}_2 + \hat{W}_\tau^T S_\tau(\hat{Z}_\tau) + \hat{W}^T S(\hat{Z}) + \bar{f} \tag{45}$$

$$\dot{\hat{W}} = -\Gamma \left(S(\hat{Z}) \hat{z}_2 + \theta \hat{W} \right) \tag{46}$$

$$\dot{\hat{W}}_\tau = -\Gamma_\tau \left(S_\tau(\hat{Z}_\tau) \hat{z}_2 + \theta_\tau \hat{W}_\tau \right). \tag{47}$$

The neural network inputs are set as $\hat{Z} = [x_1^T, \hat{x}_2^T, \dot{q}_r^T, \ddot{q}_r^T]$, $\hat{Z}_\tau = [\tau^T, x_1^T, \hat{x}_2^T]$. The overall control strategy for output feedback control is illustrated in Fig. 6.

Considering (37), (45)–(47), we have

$$\begin{aligned}\dot{V}_2 =& -z_1^T \Lambda z_1 - z_1^T \eta_l - z_2^T K_2 \hat{z}_2 + z_2^T \Big(\hat{W}_\tau^T S_\tau(\hat{Z}_\tau) - \epsilon_\tau \\ & - W_\tau^{*T} S_\tau(Z_\tau) + \hat{W}^T S(\hat{Z}) - W^{*T} S(Z) \\ & - \epsilon + \bar{f} - f_{\text{dis}} \Big).\end{aligned} \tag{48}$$

Let estimation error $\tilde{z}_2 = \hat{z}_2 - z_2$, and add the effects of $\hat{W}$ and $\hat{W}_\tau$ on the stability. $V_2^* = V_2 + \frac{1}{2}\sum_{i=1}^n \tilde{W}_i^T \Gamma_i^{-1} \tilde{W}_i + \frac{1}{2}\sum_{j=1}^n \tilde{W}_{\tau,j}^T \Gamma_{\tau,j}^{-1} \tilde{W}_{\tau,j}$. Considering $\tilde{W} = \hat{W} - W^*$ and $\tilde{W}_\tau = \hat{W}_\tau - W_\tau^*$ and substituting updating law (46) and (47), we have

$$\begin{aligned}\dot{V}_2^* =& -z_1^T \Lambda z_1 - z_1^T \eta_l - z_2^T K_2 z_2 - z_2^T K_2 \tilde{z}_2 + z_2^T (\bar{f} - f_{\text{dis}}) \\ & - z_2^T (\epsilon + \epsilon_\tau) + z_2^T \Big(W_\tau^{*T} (S_\tau(\hat{Z}_\tau) - S_\tau(Z_\tau)) \\ & + W^{*T} (S(\hat{Z}) - S(Z)) \Big) - \sum_{i=1}^n \tilde{z}_{2,i} \tilde{W}_i^T S_i(\hat{Z}) \\ & - \sum_{j=1}^n \tilde{z}_{2,j} \tilde{W}_{\tau,j}^T S_{\tau,j}(\hat{Z}_\tau) - \sum_{i=1}^n \theta_i \tilde{W}_i^T \hat{W}_i \\ & - \sum_{j=1}^n \theta_{\tau,j} \tilde{W}_{\tau,j}^T \hat{W}_{\tau,j}.\end{aligned} \tag{49}$$

Consider the effect of estimation error $\tilde{z}_2$, $V = V_2^* + V_{\text{obs}}$ and $V_{\text{obs}} = \frac{1}{2}\tilde{z}_2^T\tilde{z}_2$. Based on [33], we have

$$V_{\text{obs}} \leq \frac{1}{2}\gamma^2 h_2^2. \tag{50}$$

We just need to check the stability condition of V_2^* term as V_{obs} is stable. According to [33], we have $S_i(\hat{Z}) - S_i(Z) = \bar{\gamma}S_{ti}$, $S_{\tau,j}(\hat{Z}_\tau) - S_{\tau,j}(Z_\tau) = \bar{\gamma}_\tau S_{\tau,tj}$, where $\boldsymbol{S}_{ti}$ and $\boldsymbol{S}_{\tau,tj}$ are bounded vector functions and $\bar{\gamma} > 0$. According to Assumption 1, we conclude that $\bar{f} - f_{\text{dis}} \leq 2\bar{f}$.

Since $-\tilde{W}_i^T\hat{W}_i = -\tilde{W}_i^T(W_i^* + \tilde{W}_i) = -\tilde{W}_i^T\tilde{W}_i - \tilde{W}_i^T W_i^*$ and $-\tilde{W}_i^T W_i^* \leq \frac{1}{2}(\tilde{W}_i^T\tilde{W}_i + W_i^{*T}W_i^*)$, we have $-\tilde{W}_i^T\hat{W}_i \leq -\frac{1}{2}\tilde{W}_i^T\tilde{W}_i + \frac{1}{2}W_i^{*T}W_i^*$. Similarly, $-\tilde{W}_{\tau,j}^T\hat{W}_{\tau,j} \leq -\frac{1}{2}\tilde{W}_{\tau,j}^T\tilde{W}_{\tau,j} + \frac{1}{2}W_{\tau,j}^{*T}W_{\tau,j}^*$, and $-z_1^T\eta_l \leq \frac{1}{2}(z_1^T z_1 + \eta_l^T\eta_l)$, $-z_2^T\epsilon - z_2^T\epsilon_\tau \leq z_2^T z_2 + \frac{1}{2}\epsilon^T\epsilon + \frac{1}{2}\epsilon_\tau^T\epsilon_\tau$, $-z_2^T K_2\tilde{z}_2 \leq \frac{1}{2}z_2^T z_2 + \frac{1}{2}\tilde{z}_2^T K_2^T K_2\tilde{z}_2$, $z_2^T(\bar{f} - f_{\text{dis}}) \leq z_2^T z_2 + \bar{f}^T\bar{f}$. Substituting these inequalities into (49), we have

$$\begin{aligned}
\dot{V}_2^* \leq & -z_1^T(\Lambda - \frac{1}{2}I_{n\times n})z_1 - z_2^T(K_2 - \frac{5}{2}I_{n\times n})z_2 \\
& + \frac{1}{2}\tilde{z}_2^T K_2^T K_2\tilde{z}_2 + \frac{1}{2}\eta_l^T\eta_l + \frac{1}{2}\epsilon_\tau^T\epsilon_\tau + \frac{1}{2}\epsilon^T\epsilon + \bar{f}^T\bar{f} \\
& + \sum_{i=1}^{n}\Big(z_{2,i}W_i^*\bar{\gamma}S_{ti} - \tilde{z}_{2,i}\tilde{W}_i^T S_i(\hat{Z}) - \frac{1}{2}\theta_i\tilde{W}_i^T\tilde{W}_i \\
& + \frac{1}{2}\theta_i W_i^{*T}W_i^*\Big) + \sum_{j=1}^{n}\big(z_{2,j}W_{\tau,j}^*\bar{\gamma}_\tau S_{\tau,tj} \\
& - \tilde{z}_{2,j}\tilde{W}_{\tau,j}^T S_{\tau,j}(\hat{Z}_\tau) - \frac{1}{2}\theta_{\tau,j}\tilde{W}_{\tau,j}^T\tilde{W}_{\tau,j} \\
& + \frac{1}{2}\theta_{\tau,i}W_{\tau,j}^{*T}W_{\tau,j}^*\Big)
\end{aligned} \tag{51}$$

where ϵ, ϵ_τ, and η_l satisfy $\max_{Z\in\Omega_z}\|\epsilon\| < \epsilon^*$, $\max_{Z_\tau\in\Omega_z}\|\epsilon_\tau\| < \epsilon_\tau^*$, $\max_{Z\in\Omega_z}\|\eta_l\| < \eta_l^*$, respectively, since

$$z_{2,i}W_i^*\bar{\gamma}S_{ti} \leq \frac{1}{2}z_{2,i}^2 + \frac{1}{2}\|\bar{\gamma}S_{ti}\|^2\|W_i^*\|^2 \tag{52}$$

$$z_{2,j}W_{\tau,j}^*\bar{\gamma}S_{\tau,tj} \leq \frac{1}{2}z_{2,j}^2 + \frac{1}{2}\|\bar{\gamma}_\tau S_{\tau,tj}\|^2\|W_{\tau,j}^*\|^2. \tag{53}$$

Considering $\|S_i(\hat{Z}_i)\|^2 \leq l_i$ and $\|S_{\tau,j}(\hat{Z}_{\tau,j})\|^2 \leq l_{\tau,j}$, we have

$$\begin{aligned}
-\tilde{z}_{2,i}\tilde{W}_i^T S_i(\hat{Z}) \leq & \frac{\theta_i}{4}\|\tilde{W}_i\|^2 + \frac{2l_i}{2\theta_i}\tilde{z}_{2,i}^2 \\
= & \frac{\theta_i}{4}\|\tilde{W}_i\|^2 + \frac{2l_i}{\theta_i}\frac{1}{2}\tilde{z}_{2,i}^2
\end{aligned} \tag{54}$$

$$\begin{aligned}
-\tilde{z}_{2,j}\tilde{W}_{\tau,j}^T S_{\tau,j}(\hat{Z}_\tau) \leq & \frac{\theta_{\tau,j}}{4}\|\tilde{W}_{\tau,j}\|^2 + \frac{2l_{\tau,j}}{2\theta_{\tau,j}}\tilde{z}_{2,j}^2 \\
= & \frac{\theta_{\tau,j}}{4}\|\tilde{W}_{\tau,j}\|^2 + \frac{2l_{\tau,j}}{\theta_{\tau,j}}\frac{1}{2}\tilde{z}_{2,j}^2.
\end{aligned} \tag{55}$$

Substituting (52), (53)–(55) into (55), we have

$$\begin{aligned}
\dot{V}_2^* \leq & -z_1^T(\Lambda - \frac{1}{2}I_{n\times n})z_1 - z_2^T(K_2 - \frac{7}{2}I_{n\times n})z_2 \\
& - \sum_{i=1}^{n}\frac{\theta_i}{4}\|\tilde{W}_i\|^2 - \sum_{j=1}^{n}\frac{\theta_{\tau,j}}{4}\|\tilde{W}_{\tau,j}\|^2 \\
& + \sum_{i=1}^{n}\frac{\bar{\gamma}^2\|S_{ti}\|^2 + \theta_i}{2}\|W_i^*\|^2 \\
& + \sum_{j=1}^{n}\frac{\bar{\gamma}_\tau^2\|S_{\tau,tj}\|^2 + \theta_{\tau,j}}{2}\|W_{\tau,j}^*\|^2 + \frac{1}{2}\epsilon^T\epsilon \\
& + \frac{1}{2}\epsilon_\tau^T\epsilon_\tau + \frac{1}{2}\eta_l^T\eta_l + \bar{f}^T\bar{f} \\
& + \frac{1}{2}\left(K_2^T K_2 + \Phi + \Phi_\tau\right)\|\gamma h_2\|^2 \\
\leq & -\kappa V_2^* + B
\end{aligned} \tag{56}$$

where $\kappa = \min\Big(2\lambda_{\min}(\Lambda - \frac{1}{2}I_{n\times n}), \frac{2\lambda_{\min}(K_2 - \frac{7}{2}I_{n\times n})}{\lambda_{\max}(M)}, \min_{i=1,2,\ldots,n}\left\{\frac{2\theta_i}{4\lambda_{\max}(\Gamma_i^{-1})}\right\}, \min_{j=1,2,\ldots,n}\left\{\frac{2\theta_{\tau,j}}{4\lambda_{\max}(\Gamma_{\tau,j}^{-1})}\right\}\Big)$, and $B = \sum_{i=1}^{n}\frac{\bar{\gamma}^2\|S_{ti}\|^2 + \theta_i}{2}\|W_i^*\|^2 + \frac{1}{2}\|\epsilon^*\|^2 + \frac{1}{2}\|\epsilon_\tau^*\|^2 + \frac{1}{2}\|\eta_l^*\|^2 + \|\bar{f}\|^2 + \frac{1}{2}\left(K_2^T K_2 + \Phi + \Phi_\tau\right)\|\gamma h_2\|^2 + \sum_{j=1}^{n}\frac{\bar{\gamma}_\tau^2\|S_{\tau,tj}\|^2 + \theta_{\tau,j}}{2}\|W_{\tau,j}^*\|^2$, $\Phi = \text{diag}[\frac{2l_i}{\theta_i}]$, $\Phi_\tau = \text{diag}[\frac{2l_{\tau,j}}{\theta_{\tau,j}}]$.

To guarantee $\kappa > 0$, the design parameters $\theta_i > 0$, $\theta_{\tau,j} > 0$, $\Lambda - \frac{1}{2}I_{n\times n} = (\Lambda - \frac{1}{2}I_{n\times n})^T > 0$ and $K_2 - \frac{7}{2}I_{n\times n} = \left(K_2 - \frac{7}{2}I_{n\times n}\right)^T > 0$. In the end, we have the following theorem.

Theorem 1: Considering the robotic exoskeleton system (19) with the unknown disturbances and deadzones which fulfills the Assumption 3 with known and smooth reference trajectory. The proposed output feedback control (45), neural network updating laws (46), (47) with bounded initial conditions, the closed-loop system signals, z_1 z_2, $\tilde{W}$, $\tilde{W}_\tau$, and estimation error $\tilde{z}_2$ are semiglobally bounded. Furthermore, the closed-loop error signals z_1, z_2, $\tilde{W}$, and $\tilde{W}_\tau$ will remain within the compact sets Ω_{z1}, Ω_{z2}, $\Omega_{\tilde{W}}$, $\Omega_{\tilde{W}_\tau}$, respectively, defined by $\Omega_{z1} = \left\{z_1 \in \mathbb{R}^n | \quad \|z_{1i}\| \leq \sqrt{D}\right\}$, $\Omega_{z2} = \left\{z_2 \in \mathbb{R}^n | \quad \|z_{2i}\| \leq \sqrt{\frac{D}{\lambda_{\min}(M)}}\right\}$, $\Omega_{\tilde{W}} = \left\{\tilde{W} \in \mathbb{R}^n | \quad \|\tilde{W}_i\| \leq \sqrt{\frac{D}{\lambda_{\min}(\Gamma^{-1})}}\right\}$, $\Omega_{\tilde{W}_\tau} = \left\{\tilde{W}_\tau \in \mathbb{R}^n | \quad \|\tilde{W}_{\tau,j}\| \leq \sqrt{\frac{D}{\lambda_{\min}(\Gamma_\tau^{-1})}}\right\}$, where $D = 2\left(V_2^*(0) + \frac{B}{\kappa}\right)$ with κ and B given in (56).

Proof: Multiplying (56) by $e^{\kappa t}$ yields $\frac{d}{dt}(V_2^* e^{\kappa t}) \leq Be^{\kappa t}$. Integrating the above inequality, we have $V_2^* \leq \left(V_2^*(0) - \frac{B}{\kappa}\right)e^{-\kappa t} + \frac{B}{\kappa} \leq V_2^*(0) + \frac{B}{\kappa}$. For z_1, we have $\frac{1}{2}z_1^T z_1 \leq V_2^*(0) + \frac{B}{\kappa}$. Then, we can obtain $||z_1||^2 \leq 2(V_2^*(0) + \frac{B}{\kappa})$. For z_2, we have $\frac{1}{2}z_2^T M z_2 \leq V_2^*(0) + \frac{B}{\kappa}$. Then, we can obtain $||z_2||^2 \leq 2\frac{V_2^*(0) + \frac{B}{\kappa}}{\lambda_{\min}(M)}$. As for $\tilde{W}$, we have $\frac{1}{2}\tilde{W}^T\Gamma^{-1}\tilde{W} \leq V_2^*(0) + \frac{B}{\kappa_1}$. Then, we have $||\tilde{W}||^2 \leq \frac{2(V_2^*(0) + \frac{B}{\kappa})}{\lambda_{\min}(\Gamma^{-1})}$. As for, $\tilde{W}_\tau$ we can obtain $\frac{1}{2}\tilde{W}_\tau^T\Gamma_\tau^{-1}\tilde{W}_\tau \leq V_2^*(0) + \frac{B}{\kappa_1}$. Finally, we have $||\tilde{W}_\tau||^2 \leq \frac{2(V_2^*(0) + \frac{B}{\kappa})}{\lambda_{\min}(\Gamma_\tau^{-1})}$. ■

V. Experimental Studies

First, the subject is involved in the experiment of impedance parameters' identification. In Fig. 1, from the processed sEMG of each muscle, u_i derived the muscle activations a_i, and then the muscle–tendon forces $F_i^{mt}(t)$ would produce the net torque τ_{net} and the joint stiffness trend STI. Two antagonistic muscle pairs denoted as being the dominant surface muscles acting on the shoulder and elbow joints were chosen to obtain the musculoskeletal model. The electrodes were attached to the biceps long head (BILH), triceps medial head (TRIM), pectoralis major clavicular part (PMJC), and deltoid scapular part (DELS) muscles. The raw sEMG signals need to be processed by high-pass filtering, full-wave rectification, low-pass filtering, and then normalized with respect to the muscle's MVC level. To identify the parameters α_l and β_l in (11), the subject is instructed to keep muscles tightened, and the joint torques and STI parameters are obtained through the sEMG-driven musculoskeletal model. After acquiring the joint torques and STI parameters, we measure the joint stiffness of the human forearm's joints through a 6-axis force-torque sensor and the sEMG signals. Then, the calculated joint stiffness could be fitted to the function of STI; α_l and β_l in (11) could be identified. After constructing the targeted impedance model, we employ the shoulder and elbow joints of the robot to conduct experiment. The upper limb exoskeleton tracks the designed trajectories which are selected as $q_1 = 0.5\sin(t)$ and $q_2 = 0.5\sin(t)$.

The design parameters are $M_r = \text{diag}[0.47, 0.50]$, and K_r, C_r, F_r are acquired from the identified parameters $K_l, C_l, \tau_{\text{joint}}$. The asymmetrical and unknown deadzone is defined as $b_{l1} = -0.5, b_{r1} = 0.5, b_{l2} = -0.3, b_{r2} = 0.3$. The deadzone nonlinearity in the robotic exoskeleton can be described as $h_r(\tau) = (1 - 0.3\sin(\tau))(\tau - b_r)$ and $h_r(\tau) = (0.8 - 0.2\cos(\tau))(\tau + b_l)$, $\bar{f} = 2.0$. A total of $N = 2^8$ nodes are used for the RBFNN $W^T S(Z)$. The centers are evenly distributed in: $[-0.5, 0.5] \times [-0.5, 0.5] \times [-0.5, 0.5] \times [-0.5, 0.5] \times [-0.5, 0.5] \times [-0.5, 0.5] \times [-0.5, 0.5] \times [-0.5, 0.5] \times$ with each parameter either be -0.5 or 0.5. 2^6 nodes are used for the RBFNN $W_\tau^T S_\tau(Z_\tau)$. Centers of S_τ are evenly distributed in the space of $[-0.5, 0.5] \times [-0.5, 0.5] \times [-0.5, 0.5] \times [-0.5, 0.5] \times [-0.5, 0.5] \times [-0.5, 0.5]$. Parameters in neural network updating laws are set to $\Gamma_1 = 0.001, \Gamma_2 = 0.001, \Gamma_{\tau,1} = 0.001, \Gamma_{\tau,2} = 0.001$. Small positive constants are chosen as $\theta_1 = 0.2, \theta_2 = 0.2, \theta_{\tau,1} = 0.1, \theta_{\tau,2} = 0.1$. Initial weights $\hat{W}_{N,j} = 0 (j = 1, 2; N = 1, 2, 3, 4, \ldots, 2^8)$ and $\hat{W}_{\tau,N,j} = 0 (j = 1, 2; N = 1, 2, 3, 4, \ldots, 2^6)$, $\epsilon^* = 0.5$. The control gains are given as $K_2 = \text{diag}[2.514, 2.54]$. The design parameters involved in the high-gain observer term are $\varepsilon = 0.015$ and $\lambda = [2.25, 2.25]^T$, and initial terms $\pi_{1o} = [0, 0]^T, \pi_{2o} = [0, 0]^T, \dot{\pi}_{1o} = [0, 0]^T$ and $\dot{\pi}_{2o} = [0, 0]^T, \hat{Z} = [x_1^T, \hat{x}_2^T, \dot{q}_r^T, \ddot{q}_r^T]^T$, and $\hat{Z}_\tau = [\tau^T, x_1^T, \hat{x}_2^T]^T$.

The estimated joint stiffness for two joints are shown in Figs. 7 and 8. The desired trajectories and actual trajectories for two joints are shown in Figs. 9 and 10. The two figures illustrate that the actual position can converge to the desired trajectories with small and bounded errors. The tracking errors for shoulder and elbow joints are shown in Fig. 11. It can be seen that the tracking errors are converging smaller with the time. Fig. 12 shows the evolution of the input currents for the corresponding motors.

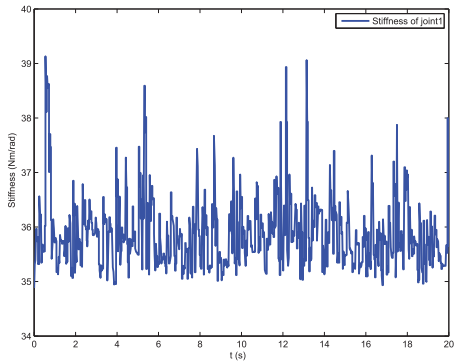

Fig. 7. Estimated stiffness of joint1 (unit: Nm/rad).

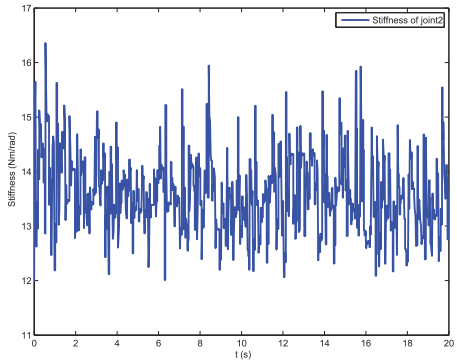

Fig. 8. Estimated stiffness of joint2 (unit: Nm/rad).

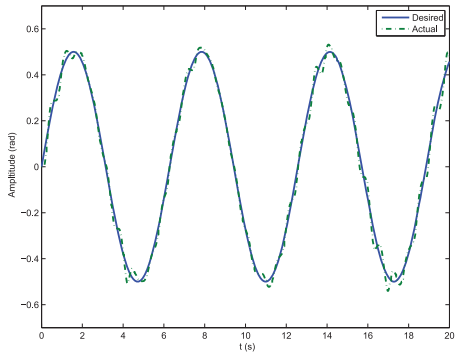

Fig. 9. Trajectory tracking of the joint 1 (unit: rad).

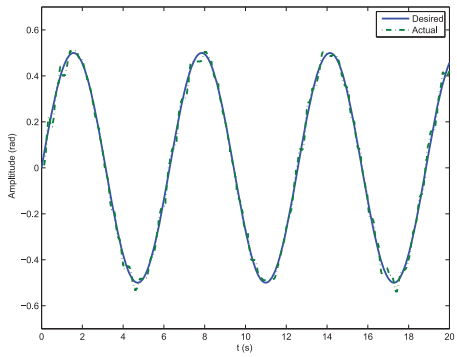

Fig. 10. Trajectory tracking of the joint 2 (unit: rad).

From these figures, even though in the case of the absence of the precise knowledge of dynamics of the robotic exoskeleton, we could still achieve desired performance by the proposed control scheme. From the experiments, we can see that the

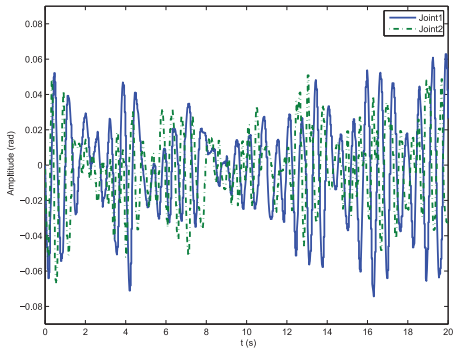

Fig. 11. Error trajectories of the joints 1 and 2 (unit: rad).

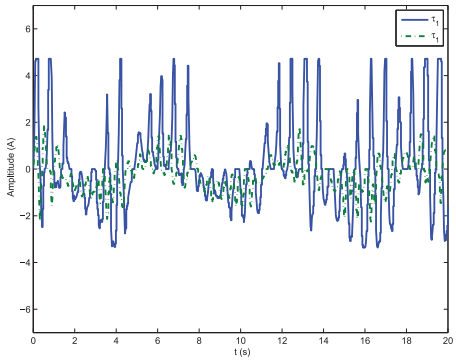

Fig. 12. Driving motor currents of the joints 1 and 2 (unit: A).

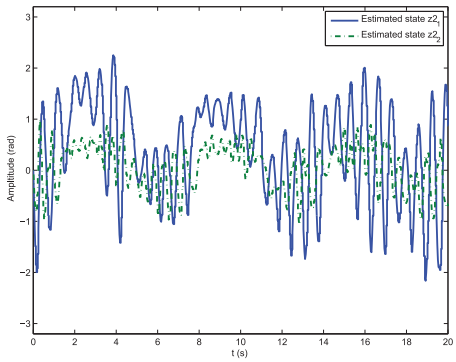

Fig. 13. The estimated state of z_2 (Unit: rad).

actual position converges to the desired trajectory in Figs. 9 and 10, and input currents are bounded and stable as shown in Fig. 12. The estimated state of z_2 is shown in Fig. 13.

VI. Conclusion

This paper has presented a method of implementing the adaptive impedance control for the upper limb exoskeleton robot using biological signals. First, we have adopted the sEMG-driven musculoskeletal model to acquire the joint stiffness, viscosity parameters, and the net torques of the human forearm. Then, by utilizing the model reference approach, the dynamics of upper limb exoskeleton system has been shaped to match the desired impedance model, which is derived by identification of the human limb's impedance parameters through sEMG signals. The proposed control incorporating RBFNNs is employed for the exoskeleton to drive the robotic exoskeleton tracking the desired trajectories. In our future work, we shall consider the viable stiffness in the human limb model and incorporate the stiffness property into the control design of the robotic exoskeleton. In addition, we shall also conduct the extensive experiments to verify the designed viable stiffness controller.

References

[1] R. Lu, Z. Li, C.-Y. Su, and A. Xue, "Development and learning control of a human limb with a rehabilitation exoskeleton," *IEEE Trans. Ind. Electron.*, vol. 61, no. 7, pp. 3776–3785, Jul. 2014.

[2] Z. Li, C.-Y. Su, L. Wang, Z. Chen, and T. Chai, "Nonlinear disturbance observer design for a robotic exoskeleton incorporating fuzzy approximation," *IEEE Trans. Ind. Electron.*, vol. 62, no. 9, pp. 5763–5775, Sep. 2015.

[3] E. Burdet, G. Ganesh, C. Yang, and A. Albu-Schaffer, "Interaction force, impedance and trajectory adaptation: By humans, for robots," in *Experimental Robotics*. New York, NY, USA: Springer, 2014, vol. 79, pp. 331–345.

[4] J. Ueda, D. Ming, V. Krishnamoorthy, M. Shinohara, and T. Ogasawara, "Individual muscle control using an exoskeleton robot for muscle function testing," *IEEE Trans. Neural Syst. Rehabil. Eng.*, vol. 18, no. 4, pp. 339–350, Aug. 2010.

[5] K. P. Tee, D. Franklin, M. Kawato, T. Milner, and E. Burdet, "Concurrent adaptation of force and impedance in the redundant muscle system," *Biol. Cybern.*, vol. 102, no. 1, pp. 31–44, 2010.

[6] E. Burdet *et al.*, "Stability and motor adaptation in human arm movements," *Biol. Cybern.*, vol. 94, no. 1, pp. 20–32, 2006.

[7] W. He, Y. Dong, and C. Sun, "Adaptive neural impedance control of a robotic manipulator with input saturation," *IEEE Trans. Syst. Man Cybern. Syst.*, vol. 46, no. 3, pp. 334–344, Mar. 2016, doi: 10.1109/TSMC.2015.2429555.

[8] V. Panwara, N. Kumarb, N. Sukavanamc, and J.-H. Bormb, "Adaptive neural controller for cooperative multiple robot manipulator system manipulating a single rigid object," *Appl. Soft Comput.*, vol. 12, no. 1, pp. 216–227, Jan. 2012.

[9] B. Xu, S. R. Pandian, N. Sakagami, and F. Petry, "Neuro-fuzzy control of underwater vehicle-manipulator systems," *J. Franklin Inst.*, vol. 349, no. 3, pp. 1125–1138, Apr. 2012.

[10] Z. Li, S. Xiao, S. S. Ge, and H. Su, "Constrained multi-legged robot system modeling and fuzzy control with uncertain kinematics and dynamics incorporating foot force optimization," *IEEE Trans. Syst. Man Cybern., Syst.*, vol. 46, no. 1, pp. 1–15, Jan. 2016.

[11] M.-B. Cheng, W.-C. Su, C.-C. Tsai, and T. Nguyen, "Intelligent tracking control of a dual-arm wheeled mobile manipulator with dynamic uncertainties," *Int. J. Robust Nonlinear Control*, vol. 23, no. 8, pp. 839–857, May 2013.

[12] T. Lenzi, S. M. M. De Rossi, N. Vitiello, and M. C. Carrozza, "Intention-based EMG control for powered exoskeletons," *IEEE Trans. Biomed. Eng.*, vol. 59, no. 8, pp. 2180–2190, Aug. 2012.

[13] K. Kiguchi and Y. Hayashi, "An EMG-based control for an upper-limb power-assist exoskeleton robot," *IEEE Trans. Syst. Man Cybern. B, Cybern.*, vol. 42, no. 4, pp. 1064–1071, Aug. 2012.

[14] S. Lee and Y. Sankai, "Power assist control for walking aid based on EMG and impedance adjustment with HAL-3 around knee joint," in *Proc. IEEE/RSJ Int. Conf. Intell. Robots Syst.*, 2002, vol. 2, pp. 1499–1504.

[15] D. Shin, J. Kim, and Y. Koike, "A myokinetic arm model for estimating joint torque and stiffness from EMG signals during maintained posture," *J. Neurophysiol.*, vol. 101, pp. 387–401, 2009.

[16] A. Ajoudani, N. Tsagarakis, and A. Bicchi, "Tele-impedance: Teleoperation with impedance regulation using a body-machine interface," *Int. J. Robot. Res.*, vol. 31, no. 13, pp. 1642–1655, 2012.

[17] C. Fleischer and G. Hommel, "A human-exoskeleton interface utilizing electromyography," *IEEE Trans. Robot.*, vol. 24, no. 4, pp. 872–882, Aug. 2008.

[18] N. Hogan, "Impedance control: An approach to manipulation-part I: theory; part II: implementation; part III: applications," *Trans. ASME, J. Dyn. Syst., Meas. Control*, vol. 107, no. 1, pp. 1–24, 1985.

[19] Z. Li, C. Yang, C.-Y. Su, and W. Ye, "Adaptive fuzzy-based motion generation and control for mobile underactuated manipulators," *Eng. Appl. Artif. Intell.*, vol. 30, pp. 86–95, Apr. 2014.

[20] Z. Liu, F. Wang, and Y. Zhang, "Adaptive visual tracking control for manipulator with actuator fuzzy dead-zone constraint and unmodeled dynamic," *IEEE Trans. Syst. Man Cybern., Syst.*, vol. 45, no. 10, pp. 1301–1312, Oct. 2015.
[21] K. P. Tee and S. S. Ge, "Control of fully actuated ocean surface vessels using a class of feedforward approximators," *IEEE Trans. Control Syst. Technol.*, vol. 14, no. 4, pp. 750–756, Jul. 2006.
[22] F. E. Zajac, "Muscle and tendon: Properties, models, scaling, and application to niomechanics and motor control," *Crit. Rev. Biomed. Eng.*, vol. 17, pp. 359–411, 1989.
[23] D. G. Lloyd and T. E. Bessier, "An EMG-driven musculoskeletal model to estimate muscle forces and keen joint moments in vivo," *J. Biomech.*, vol. 36, no. 6, pp. 765–776, Jun. 2003.
[24] J. Han, Q. Ding, A. Xiong, and X. Zhao, "A state-space EMG model for the estimation of continuous joint movements," *IEEE Trans. Ind. Electron.*, vol. 62, no. 7, pp. 4267–4275, Jul. 2015.
[25] Q. C. Ding, A. B. Xiong, X. G. Zhao, and J. D. Han, "A novel EMG-driven state space model for the estimation of continuous joint movements," in *Proc. IEEE Int. Conf. Syst. Man Cybern.*, 2011, pp. 2891–2897.
[26] P. A. Huijing, "Important experimental factors for skeletal muscle modelling: Non-linear changes of muscle length force characteristics as a function of degree of activity," *Eur. J. Morphol.*, vol. 34, no. 1, pp. 47–54, 1996.
[27] K. N. An, K. Takahashi, T. P. Harrigan, and E. Y. Chao, "Determination of muscle orientations and moment arms," *J. Biomech. Eng.*, vol. 106, pp. 280–282, Aug. 1984.
[28] R. Osu and H. Gomi, "Multi-joint muscle regulation mechanisms examined by measured human-arm stiffness and EMG signals," *J. Neurophysiol.*, vol. 81, pp. 1458–1468, 1999.
[29] H. Gomi and R. Osu, "Task-dependent viscoelasticity of human multijoint arm and its spatial characteristics for interaction with environments," *J. Neurosci.*, vol. 18, pp. 8965–8978, 1998.
[30] R. Osu *et al.*, "Short- and long-term changes in joint co-contraction associated with motor learning as revealed from surface EMG," *J. Neurophysiol.*, vol. 88, no. 5, pp. 991–1004, 2002.
[31] P. Liang, C. Yang, N. Wang, Z. Li, R. Li, and E. Burdet, "Implementation and test of human-operated and human-like adaptive impedance controls on baxter robot," in *Advances in Autonomous Robotics Systems*, vol. 8717, ser. Lecture Notes in Computer Science. London, U.K.: Springer, 2014, pp. 109–119.
[32] A. Ajoudani, N. G. Tsagarakis, and A. Bicchi, "Tele-impedance: Preliminary results on measuring and replicating human arm impedance in tele operated robots," in *Proc. IEEE Int. Conf. Robot. Biomimetics (ROBIO)*, 2011, pp. 216–222.
[33] S. S. Ge, T. H. Lee, and C. J. Harris, *Adaptive Neural Network Control of Robot Manipulators*. Singapore: World Scientific, 1998.
[34] S. Behtash, "Robust output tracking for nonlinear system," *Int. J. Control*, vol. 51, no. 6, pp. 931–933, 1990.

Zhijun Li (M'07–SM'09) received the Dr. Eng. degree in mechatronics from Shanghai Jiao Tong University, Shanghai, China, in 2002.

From 2003 to 2005, he was a Postdoctoral Fellow with the Department of Mechanical Engineering and Intelligent systems, University of Electro-Communications, Tokyo, Japan. From 2005 to 2006, he was a Research Fellow with the Department of Electrical and Computer Engineering, National University of Singapore, Singapore, and Nanyang Technological University, Singapore. From 2007 to 2011, he was an Associate Professor with the Department of Automation, Shanghai Jiao Tong University. In 2008, he was a Visiting Scholar at Microsoft Research Asia, Beijing, China. Since 2012, he has been a Professor with the College of Automation Science and Engineering, South China University of Technology, Guangzhou, China. In 2015, he was a Visiting Professor at the Faculty Science and Technology, University of Macau, Macau, China, and the Department of Advanced Robotics, Italian Institute of Technology, Genoa, Italy. His research interests include service robotics, teleoperation systems, nonlinear control, and neural network optimization.

Dr. Li is serving as an Editor-at-Large of the *Journal of Intelligent and Robotic Systems*, and an Associate Editor of the IEEE TRANSACTIONS ON NEURAL NETWORKS AND LEARNING SYSTEMS and the IEEE TRANSACTIONS ON SYSTEMS, MAN, AND CYBERNETICS: SYSTEMS.

Zhicong Huang received the B.S. degree in control theory and engineering in 2014 from South China University of Technology, Guangzhou, China, in 2014. Currently, he is working toward the M.S. degree in the College of Automation Science and Engineering.

His research interests include exoskeleton robots and EEG signal processing.

Wei He (S'09–M'12) received the B.Eng. degree in control theory and engineering from the College of Automation Science and Engineering, South China University of Technology (SCUT), Guangzhou, China, in 2006, and the Ph.D. degree in electrical and computer engineering from the National University of Singapore (NUS), Singapore, in 2011.

From 2011 to 2012, he was a Research Fellow with the Department of Electrical and Computer Engineering, NUS. Currently, he is a Full Professor with the School of Automation and Electrical Engineering, University of Science and Technology Beijing, Beijing, China. His research interests include robotics, distributed parameter systems, and intelligent control systems.

Dr. He served as an Editor of the *Journal of Intelligent and Robotic Systems*.

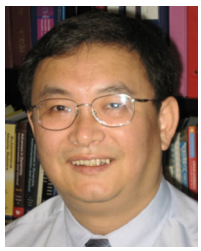

Chun-Yi Su (SM'99) received the Ph.D. degree in control engineering from South China University of Technology, Guangzhou, China, in 1990.

After a seven-year stint at the University of Victoria, he joined Concordia University, Montreal, QC, Canada, in 1998. Currently, he is with the College of Automation Science and Engineering, South China University of Technology, on leave from Concordia University. He is the author or coauthor of more than 300 publications, which have appeared in journals, as book chapters, and in conference proceedings. His research interests include the application of automatic control theory to mechanical systems and control of systems involving hysteresis nonlinearities.

Dr. Su has served as an Associate Editor of the IEEE TRANSACTIONS ON AUTOMATIC CONTROL, IEEE TRANSACTIONS ON CONTROL SYSTEMS TECHNOLOGY, and *Journal of Control Theory and Applications*. He has been on the Editorial Board of 18 journals, including *the IFAC journals Control Engineering Practice* and *Mechatronics*. He has also severed many conferences as an Organizing Committee Member, including General Co-Chair of the 2012 IEEE International Conference on Mechatronics and Automation, and Program Chair of the 2007 IEEE Conference on Control Applications.